Defect-Level Switching for Highly Nonlinear and Hysteretic Electronic Devices

Han Yin,[1] Abinash Kumar,[2] James M. LeBeau,[2] and R. Jaramillo[2,*]

[1] *Department of Mechanical Engineering, Massachusetts Institute of Technology, Cambridge, Massachusetts 02139, USA*

[2] *Department of Materials Science & Engineering, Massachusetts Institute of Technology, Cambridge, Massachusetts 02139, USA*

(Received 16 May 2020; revised 2 December 2020; accepted 7 December 2020; published 8 January 2021)

Nonlinear and hysteretic electrical devices are needed for applications from circuit protection to next-generation computing. Widely-studied devices for resistive switching are based on mass transport, such as the drift of ions in an electric field, and on collective phenomena, such as insulator-metal transitions. We ask whether the large photoconductive response known in many semiconductors can be stimulated in the dark and harnessed to design electrical devices. We design and test devices based on photoconductive CdS, and our results are consistent with the hypothesis that resistive switching arises from point defects that switch between deep- and shallow-donor configurations: defect-level switching. This electronic device design principle, photoconductivity without photons, leverages decades of research on photoconductivity and defect spectroscopy. It is easily generalized and will enable the rational design of nonlinear hysteretic devices for future electronics.

DOI: 10.1103/PhysRevApplied.15.014014

I. INTRODUCTION

Two-terminal resistive devices are basic building blocks for electronics. Simple resistors obey Ohm's law and exhibit a linear relationship between current (I) and voltage (V). Semiconductor devices often exhibit nonlinear I-V characteristics, such as diode behavior. More complicated devices exhibit I-V behavior that is both nonlinear and hysteretic. Nonlinear hysteretic behavior is needed for many applications, including circuit protection (e.g., fuses), oscillators (e.g., Gunn diode), memory selectors (e.g., ovonic switches), and emerging concepts for computing (e.g., resistive switches) [1–4]. Research on resistive switching has expanded rapidly, as future computing applications come into view, including storage-class memory, analog and resistive computing, compute-in-memory, and neuromorphic computing [5–10]. Charge-based resistive switching has been observed in many materials, and a taxonomy has emerged to describe the different underlying mechanisms [8,10]. Most resistive switches are based on the mass transport of atoms and ions, which move in response to electrochemical forces. Other categories of charge-based resistive switching are based on collective phenomena, such as amorphous-crystalline transformations (e.g., phase-change materials) and insulator-metal transitions driven by electron-electron correlation.

Here, we introduce a mechanism of charge-based resistive switching that does not require mass transport or collective phenomena. We call it defect-level switching (DLS) because it is based on atomic structure changes around semiconductor point defects; these changes affect the transition energy levels, and thereby the electrical conductivity. The underlying mechanism is grounded in well-established semiconductor physics and is already known in a number of different material systems. DLS, therefore, presents a framework for the rational design of nonlinear hysteretic electronic devices with properties (e.g., switching speed and energy, retention time, polarity) that can be accurately predicted by theory and simulation. We illustrate this predictive design framework by describing and then experimentally demonstrating two different resistive switches—a DLS device that is in a high-conductivity ("on") state, as-fabricated and at equilibrium (like a Gunn diode), and a more traditional interface switching device that is in a low-conductivity ("off") state, as-fabricated and at equilibrium—that both rely on the same active material.

Point defects in semiconductors are characterized by their transition energy levels, the thermodynamic potentials at which their equilibrium ionization state changes. In some cases, point defects can feature multiple transition levels, widely separated in energy, due to the combined effects of charge-lattice coupling and electron-electron correlation. Such systems are often bistable, with two distinct atomic arrangements, corresponding to deep- and shallow-donor states (for n-type; acceptor for p-type), where the energies of states depend on ionization (Fig. 1). These cases of strong correlation violate the independent quasiparticle assumption that underlies semiconductor

*rjaramil@mit.edu

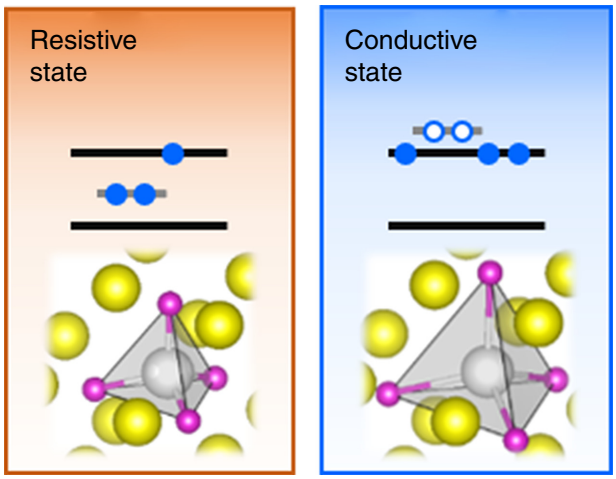

FIG. 1. Illustration of DLS. The upper illustrations are energy band diagrams with conduction band edge (upper black line), valence band edge (lower black line), defect level (gray line), electrons (full blue circles), and holes (empty blue circles). The lower illustrations are lattice configurations showing Cd atoms (purple), S atoms (yellow), and a vacant S site (gray) with its coordination environment (gray tetrahedron). Double ionization of neutral sulfur vacancies in CdS induces lattice relaxation into a metastable and highly conductive state, resulting in a billion-fold increase in conductivity upon white-light exposure [14].

electronic structure models; this is unsurprising for localized defects, the behavior of which often more closely resembles that of molecules than that of extended solids. Bistable point defects are responsible for large and persistent photoconductivity in well-studied semiconductor materials, including III-Vs (e.g., (Al, Ga)As, (Ga, In)(As, N)), II-VIs (e.g., ZnO, CdS), and chalcopyrites (e.g., $CuInS_2$, $CuGaSe_2$) [11–14].

We invite the question of whether this type and magnitude of response could be controlled in an electrical device in the dark, akin to photoconductivity, but without photons. To achieve this functionality, we need to recreate the minority carrier injection and defect ionization that occurs in photoconductivity. We use photoconductive CdS thin films as our active material and semiconductor device simulations as our design tool. For a device to be in the on state as-fabricated and at equilibrium, we require that, at zero bias, the Fermi energy (E_F) crosses the transition level of a DLS-active deep donor, resulting in level switching into a shallow-donor state and the creation of a high-conductivity sheath. The device will show resistive switching into an off state under forward bias, if the bands bend so as to reduce the width of this high-conductivity sheath.

II. METHODS

We fabricate devices on silicon wafers with an oxide layer 100 nm thick. For equilibrium-on devices, we first deposit 4 nm of Cr followed by 100 nm of Ag, using thermal evaporation. We then deposit the CdS layer by chemical bath deposition. In a typical procedure, we first dissolve 306 mg $Cd(NO_3)_2$ and 76 mg thiourea each in 10 ml deionized (DI) water, respectively. Next, we heat 76 ml DI water to 70 °C and immerse the substrate in the bath vertically. We then add chemicals to the bath in the following order: $Cd(NO_3)_2$ solution, 14 ml ammonium hydroxide, thiourea solution. The chemical bath is continuously stirred by a magnetic stirrer bar at 300 rpm, and deposition lasts for 8 min. We rinse the sample with DI water and sonicate it in isopropanol for 5 min. We then deposit 20 nm MoO_3 onto the sample using thermal evaporation, followed by a top contact layer of Cr(4 nm)/Au(50 nm).

We pattern devices using photolithography. We first spin-coat SPR 700 photoresist and then expose the pattern for 15 s using a photomask. We then develop the pattern in MF CD-26 developer for 1 min. We remove the Au top contact by ion milling, and we remove MoO_3 and CdS by etching in dilute $(NH_4)OH$ and dilute HCl, respectively. We sonicate the sample in acetone to remove the photoresist. Ion milling is necessary to remove the Au top contact because reactive etches (wet and dry) produce unwanted and messy reactions with the underlying layers.

We carry out electrical measurements using a probe station. We measure I-V data using a Keithley 2400 source meter in a two-point configuration, using Be-Cu probes to contact the devices. The substrate and top contact are connected to the low and high terminals, respectively. We use a voltage sweep rate of 0.2 V/s. The sample temperature is controlled using a thermal chuck and is set to 25 °C for all measurements, unless stated otherwise. Time series data are collected using the same source meter, with an acquisition rate of 1 Hz.

We prepare cross-section samples for electron microscopy using a Ga focused ion beam (Thermo Fisher Scientific Helios 660). We perform scanning transmission electron microscopy (STEM) characterization of devices using a probe-corrected Thermo Fisher Scientific Titan G3 60–300 kV operated at 200 kV, with a probe semiconvergence angle of 18 mrad. We perform high-angle annular dark-field imaging (HAADF), low-angle annular dark-field imaging (LAADF), and bright-field (BF) STEM imaging with detector collection angle ranges of 63–200, 15–59, and 0–13 mrad, respectively. STEM energy-dispersive spectroscopy (EDS) elemental maps are formed after background subtraction. To reduce noise, each elemental map is convolved with a two-dimensional Gaussian with three-pixel standard deviation.

III. RESULTS AND DISCUSSION

In Fig. 2(a), we show the design for the equilibrium-on device, using MoO_3 as a hole-injection layer [15, 16]. Simulations predict that this MoO_3/CdS device will

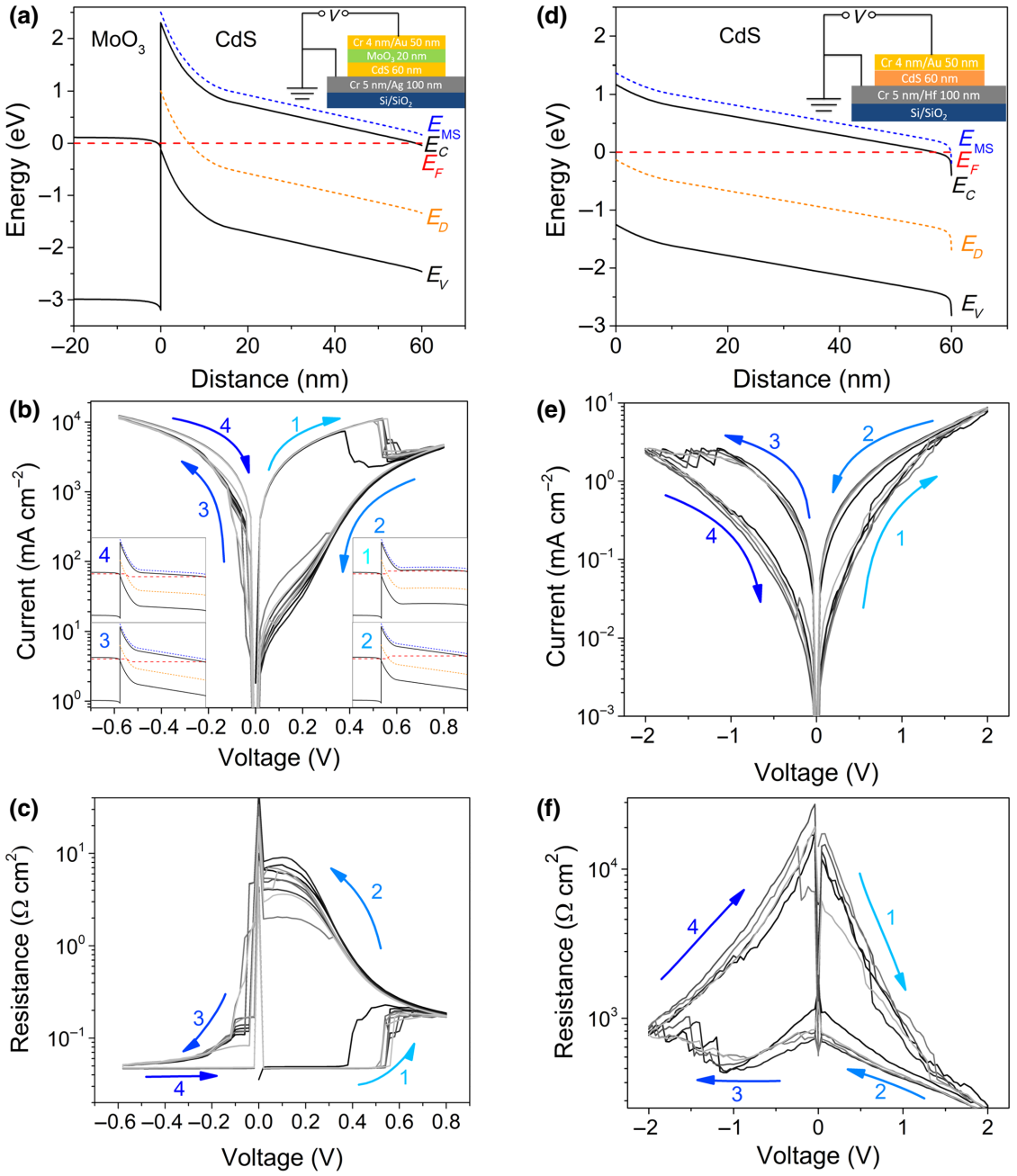

FIG. 2. Predictive design and experimental tests of DLS devices. Simulations show device band diagrams; experimental tests are on 1 mm^2 devices. E_C = conduction-band edge, E_V = valence-band edge, E_F = Fermi energy, E_D = transition energy of neutral DLS-active defect, E_{MS} = transition energy of DLS-active defect in the ionized and metastable state. (a) Design of equilibrium-on device with hole-injecting contact; simulation shows band diagram at zero bias. (b),(c) Experimental tests of equilibrium-on device. Insets in (b) are calculated band diagrams for forward and reverse bias in on and off states, corresponding to the numbered sequence 1–4, respectively. Line colors have the same meaning as those in (a). (d) Design of equilibrium-off device with inert and non-hole-injecting contacts; simulation shows band diagram at zero bias (e),(f) Experimental tests of equilibrium-off device.

switch into an off state under forward bias, as the high-conductivity sheath of ionized sulfur vacancies narrows [17]. This is remarkable because we predict that *n*-type CdS will become *less* conductive upon electron injection. In Figs. 2(b) and 2(c), we show the results of our experimental device tests; Fig. 2(b) presents measured current, and Fig. 2(c) presents the same results plotted as device resistance. The behavior is as predicted for the DLS hypothesis and device design. The device as-fabricated at equilibrium is in an on state, and the *I*-*V* curve resembles a simple resistor. Under forward bias, the device abruptly switches into a metastable off state, with a rectifying and

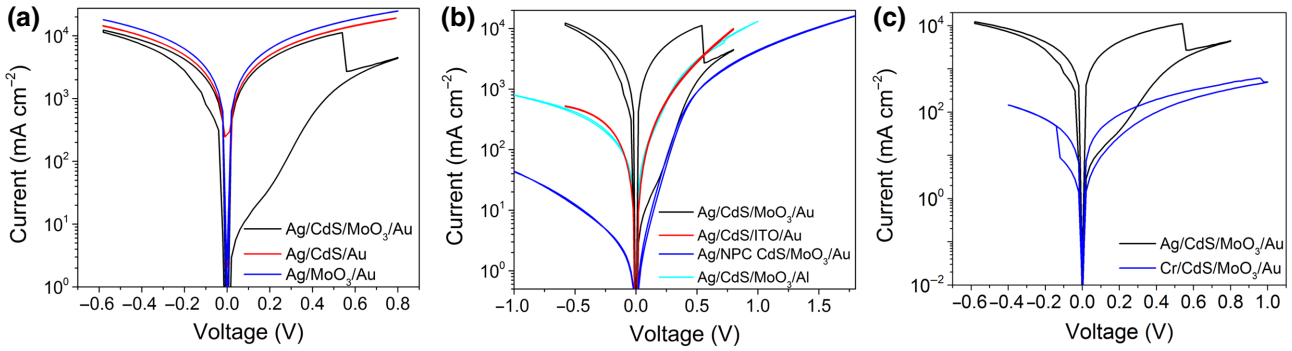

FIG. 3. Testing the DLS hypothesis by material substitution and omission. (a) Ag/CdS/Au and Ag/MoO_3/Au devices without the CdS/MoO_3 junction are simple resistors and show no switching. (b) No switching is observed for devices made using nonphotoconductive (NPC) CdS or substituting ITO in place of MoO_3. We also observe no switching for a Ag/CdS/MoO_3/Al device. (c) Equilibrium-on switching is observed for a device with Cr instead of Ag as the back contact; the quantitative differences between the Cr- and Ag-based device *I-V* curves are due to substantial series resistance contributed to by Cr.

diodelike *I-V* curve. In this state, the resistance is bias dependent, increasing at low bias [Fig. 2(c)], as expected for a $n{+}{+}/n$ junction. The original on state can be recovered by sweeping into reverse bias, like a bipolar resistive switch. The insets of Fig. 2(b) present simulated band diagrams for positive and negative bias and in the on and off states; see the Supplemental Material for a discussion of these simulations [18].

The equilibrium-on device demonstrates bipolar switching, but the switching polarity and further hypothesis tests (below) distinguish it from bipolar resistive switches based on defect motion [10]. The peculiar behavior of our equilibrium-on device is more similar to a Gunn diode. Both our devices and Gunn diodes are distinguished by a conductivity drop upon majority carrier injection, although the underlying mechanisms are different: carrier recapture at point defects in the DLS device versus injection into lower-mobility conduction-band minima in a Gunn diode. Equilibrium-on DLS devices may be useful for circuit protection (i.e., like a breaker) or as oscillators.

By selecting non-hole-injecting contacts, we can also design an equilibrium-off device. In Fig. 2(d), we show the design for an equilibrium-off device with electron-injecting Au and Hf contacts. The Au contact has a thin Cr layer that improves adhesion and suppresses possible Au migration (cf. Fig. S3 within the Supplemental Material [18]). Our design simulations predict that the DLS-active deep levels remain neutral at equilibrium and for all reasonable applied voltages; therefore, the device should be in a low-conductivity state as-fabricated, and we expect resistance switching to be controlled by defect motion at the rectifying Au/CdS junction. In Figs. 2(e) and 2(f), we show the results of our experimental device tests. The device is in a low-conductivity state at equilibrium, as predicted, and it exhibits bipolar switching between off and on states. The voltage required for switching is nearly 5 times larger than that for the equilibrium-on DLS device, and the switching polarity is consistent with mobile ionized donors that modulate the Au/CdS Schottky junction, as is widely observed in oxides [10].

The results in Fig. 2 illustrate the predictive design made possible by the DLS mechanism. We also report a number of complementary experiments with equilibrium-on devices that further test the DLS hypothesis and fall into two categories: materials processing and substitution, and advanced characterization. The most straightforward tests are those involving material omission and substitution. In Fig. 3(a), we show *I-V* data for devices with the MoO_3 or the CdS layer omitted. The resulting Ag/CdS/Au and Ag/MoO_3/Au devices are simple resistors and show no sign of resistive switching, thereby demonstrating that the MoO_3/CdS heterojunction is paramount. In Fig. 3(b), we demonstrate the joint importance of CdS photoconductivity and the MoO_3/CdS heterojunction. A device made using nonphotoconductive (NPC) CdS is rectifying and shows no switching, even for applied bias beyond ± 2 V. This demonstrates the importance of CdS photoconductivity, which derives from which derives from DLS-active sulfur vacancies [14]. Meanwhile, a device made from photoconductive CdS, but with a typical transparent conducting oxide (ITO) instead of MoO_3, is weakly rectifying and shows no resistive switching. This demonstrates the importance of the MoO_3/CdS heterojunction to imitate photoconductivity by injecting minority carriers. MoO_3 and ITO are both significantly more conductive than CdS, and therefore, the electric field inside the CdS active layer is similar during *I-V* testing for both devices. The absence of switching for the ITO/CdS device demonstrates that, although sulfur vacancies are necessary for the DLS phenomenon, their drift motion does not seem to be essential for switching. Many resistive switches are based on the formation of metal filaments in a dielectric matrix, and Ag is a widely-used filament former [8,19]. In Fig. 3(b), we present results for a Ag/CdS/MoO_3/Al device, which is

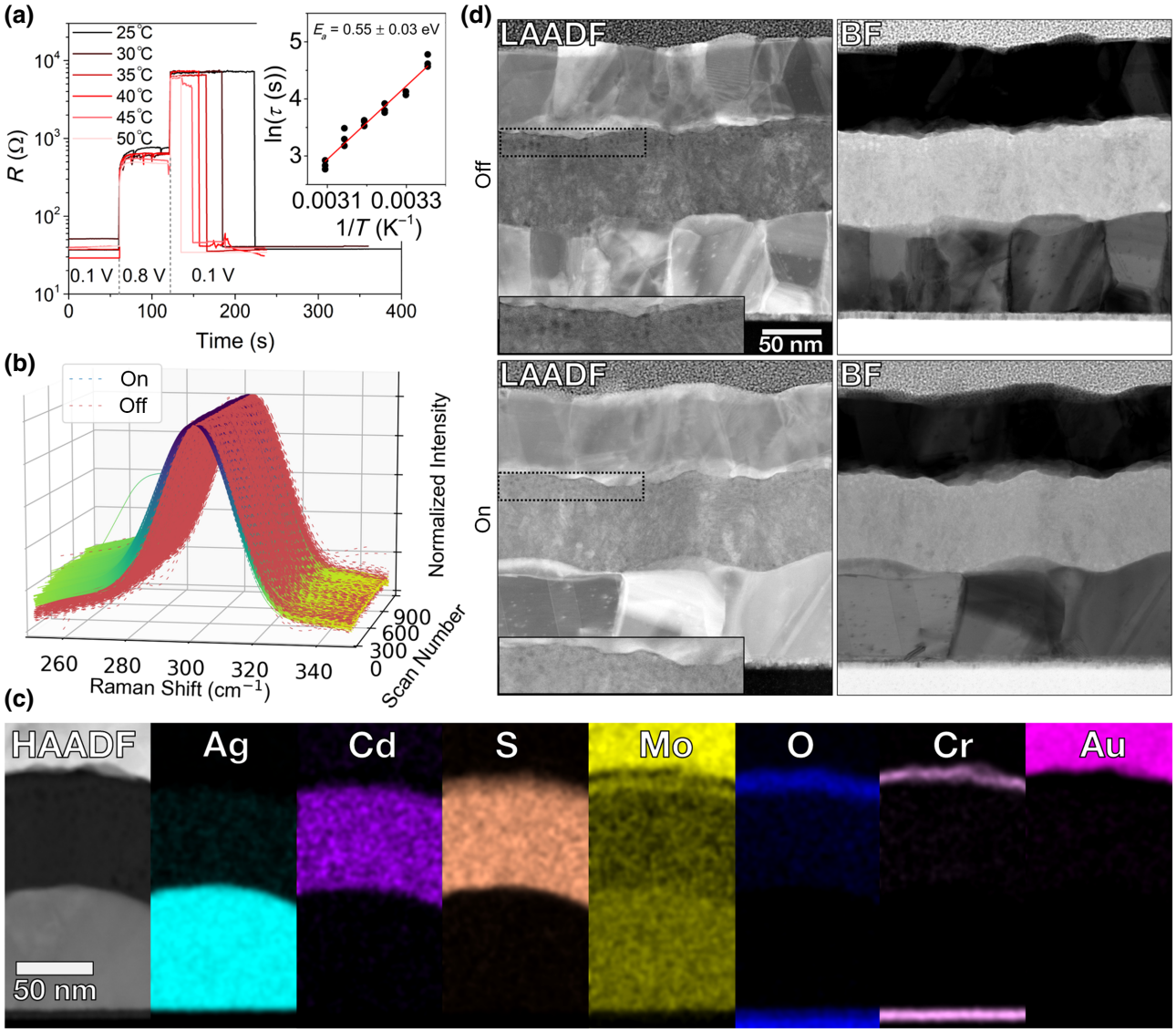

FIG. 4. Testing the DLS hypothesis by advanced characterization of equilibrium-on devices. (a) Retention kinetics show that switching between states at bistable DLS-active defects is a thermally-activated process, with an activation energy consistent with that observed for studies of photoconductivity kinetics. Main panel shows resistance as a function of time, while switching between on and off states at different temperatures. Inset shows the temperature dependence of the characteristic return-to-equilibrium time as an Arrhenius plot, with activation energy E_a; black points represent individual switching events. (b) Raman spectra acquired across $30 \times 30\ \mu m^2$ area of an equilibrium-on device with spatial resolution of $1\ \mu m^2$ show a spatially uniform blueshift of the 1LO peak upon switching from on to off, consistent with electron injection into sulfur vacancies. We plot Raman intensity as a function of Raman shift and line-scan number to best visualize the blueshift; the scan numbers correspond to 900 locations across the device area. (c) STEM EDS elemental maps showing the layer structure of a device set to the off state. Thin band of Mo is the MoO_3 layer; thick band is an artifact, due to spectral overlap with Au $M\alpha$ emission. (d) LAADF and BF images of devices set to the off state, and cycled from off to on. These images are normalized such that top Pt layer has the same brightness and contrast. The insets within the LAADF images are magnified views of the regions indicated by dashed rectangles.

weakly rectifying with no switching, due to the low work function of Al relative to that of Au. The fact that this and the Ag/CdS/Au device [Fig. 3(a)] show no switching is evidence against the role of Ag filaments in the CdS active layer. We also test for Ag filament formation by replacing Ag with relatively inert and immobile Cr. In Fig. 3(c), we show the performance of the resulting Cr/CdS/MoO_3 device, which shows the same equilibrium-on switching behavior as that of the baseline Ag/CdS/MoO_3 device. The higher bias required for switching the Cr-based device, and the lower current and relative switching magnitude (e.g., I_{on}/I_{off}), result from the substantial series resistance contributed to by the Cr bottom contact; Cr is much less conductive than Ag. By way of contrast, when we replace

Ag by Au, which is mobile and has a chemical affinity for sulfur, the resulting device performance is nonrepeatable and suggestive of both DLS and filamentary mechanisms playing a role [18]. We also find that the area-dependence of our devices is inconsistent with filamentary switching [17,20]. The results that we present in Figs. 3(a)–3(c) for alternative devices related to the baseline device by material substitution or omission (Ag/CdS/Au, Ag/MoO_3/Au, Ag/NPC-CdS/MoO_3, Ag/CdS/ITO/Au, Ag/CdS/MoO_3/Al, Cr/CdS/MoO_3/Au) are all consistent with the DLS hypothesis.

We further test the DLS mechanism by advanced characterization of equilibrium-on devices. In Fig. 4(a), we present a study of the retention kinetics. The DLS mechanism is based on the same atomic mechanism as that of photoconductivity, and we therefore expect that the kinetics of relaxation to equilibrium would be similar. We find that the time required to return to the equilibrium-on state after a switch to the off state at forward bias varies with temperature as a thermally activated process, with activation energy $E_{A,\,\mathrm{DLS}} = (0.57 \pm 0.02)$ eV. This matches the activation energy for recombination $E_{A,\,\mathrm{PC}} = (0.55 \pm 0.02)$ eV that we find in studies on CdS photoconductivity [14]. This quantitative match further supports the DLS hypothesis of resistive switching based on the same mechanism as that of photoconductivity. We note that, despite deriving from the same mechanism as photoconductivity, DLS switching can occur on a much faster timescale. The slow equilibration (hours-to-days) observed in studies on photoconductivity are typical of uniform films without electrical bias. Electrical bias accelerates processes exponentially, as the relevant quasi-Fermi levels shift relative to the relevant defects. The reversible electrical switching that we report here occurs on the timescale of rapid voltage sweeps, which is orders of magnitude faster than that of photoconductivity decay without electrical bias [14]. However, when comparing decay kinetics at zero bias [Fig. 4(a)], we recover the same activation energy as that measured for uniform film photoconductivity.

In Figure 4(b), we show Raman spectra measured across a $30 \times 30\ \mu m^2$ area of an equilibrium-on device in both the on and off states, with $1\ \mu m^2$ spatial resolution set by the excitation spot size. To make Raman spectromicroscopy possible, this device is fabricated with a semitransparent top contact. The device is electrically preconfigured before Raman measurements, which are then performed without electrical contacts and with consistent sample conditions. The excitation laser wavelength is 532 nm, which is just below the band gap of CdS. This optical excitation may perturb the on and off states that everywhere else in this report are controlled and measured all-electrically and in the dark, but we are still able to draw clear conclusions. We find that the 1LO Raman peak blueshifts uniformly by $(2.29 \pm 0.74)\ cm^{-1}$ upon switching from on to off, with no evidence of localized features (e.g., filaments) at the spatial resolution of the experiment. DLS at sulfur vacancies involves a substantial lattice strain, which may be expected to affect the phonon spectra. The blueshift in the 1LO peak position that we observe upon switching from on to off, i.e., electron injection into CdS, is consistent with a separate study of the effects of charge transfer on CdS Raman spectra; this study includes results for CdS/MoO_3 interfaces [16]. The Raman spectromicroscopy data, therefore, further support the hypothesis that resistive switching results from ionization-state transitions at sulfur vacancies, akin to photoconductivity, but engineered in an all-electrical device and without photons.

In Figs. 4(c) and 4(d), we show STEM data measured from device cross sections set to the off state and cycled between the off and on states. STEM EDS elemental maps show that all layers are coherent, with no visible interdiffusion [Fig. 4(c)]. The LAADF and BF images show that the CdS layer is dense, with no evidence of filament formation [Fig. 4(d)]. One observation is the appearance of low-density nodules within the MoO_3 layer. We speculate that these low-density regions result from electromigration of O^{2-} ions within the MoO_3 layer. It is shown that MoO_3 can exhibit interface switching due to O^{2-}-ion electromigration [21]. Although a similar phenomenon may be occurring within our devices, we note that it is distinct from the DLS mechanism that governs resistive switching in the CdS active layer. This is simply apparent from the fact that interface resistive switches based on MoO_3 are of equilibrium-off type, unlike the equilibrium-on DLS device shown here. We also recall that no resistive switching is observed in Ag/MoO_3/Au devices (Fig. 2). We adjust the images presented in Fig. 4(d) such that top Pt layer has the same brightness and contrast, which emphasizes the features in the MoO_3 layer. In the nonadjusted images (Fig. S5 within the Supplemental Material [18]), the on and off states appear more similar, further supporting our conclusion that the DLS mechanism requires no mass transport.

IV. CONCLUSION

The DLS mechanism provides a paradigm for the predictive design of nonlinear hysteretic resistive devices. It is based on the long-understood phenomenon of ionization-state transitions at bistable point defects in semiconductors and adds an extra dimension to point-defect engineering, a mainstay of semiconductor device physics. Material systems known to feature DLS phenomena include oxides (e.g., ZnO), chalcogenides (e.g., CdS, $CuInS_2$), and III-Vs (e.g., (Al, Ga)As, (Ga, In)(As, N)) and include both n-type and p-type semiconductors; in some cases, DLS may be accompanied by atomic diffusion (e.g., protons in $SrTiO_3$) [11–14,22]. Other DLS materials may be discovered by an empirical search for materials with large and persistent photoconductivity or by a heuristic search

using DFT to identify semiconductor point defects with large lattice changes upon ionization [14]. DLS does not rely on mass transport or collective phenomena, which can provide very useful device functionality, but are resistant to predictive design and often come with inherent challenges of stochasticity and fatigue. DLS devices are not bound by the voltage-time constraints that apply to devices based on deep levels that do not switch their level; modeling the switching kinetics possible with DLS devices is left to future work [23]. The design of DLS devices builds on decades of know-how in semiconductor junction and deep-level spectroscopy, and we suggest that key device properties (e.g., switching direction, speed, and energy, retention time, polarity) could be reliably predicted using well-established methods for characterizing semiconductor point defects [24].

ACKNOWLEDGMENTS

We acknowledge the following persons for informative discussions and technical assistance: Dr. Christopher Thompson (University of Delaware); Professor Marco Nardone (Bowling Green State University); Professor Nicholas Fang, Professor Jeehwan Kim, Dr. Zheng Jie Tan, Dr. Ahmed Tiamiyu, and Thomas Defferriere (MIT). Electron microscopy sample preparation is performed at the Harvard University Center for Nanoscale Systems (CNS), a member of the National Nanotechnology Coordinated Infrastructure Network (NNCI), which is supported by the National Science Foundation under NSF Grant No. 1541959. This work is supported by the Office of Naval Research MURI through Grant No. N00014-17-1-2661 and by the National Science Foundation (NSF) under Grant No. 1751736.

[1] A. Wright and P. G. Newbery, *Electric Fuses*, 3rd ed (Institution of Electrical Engineers, London, UK, 2004).

[2] P. J. Bulman, G. S. Hobson, and B. C. Taylor, *Transferred Electron Devices* (Academic Press, London, New York, 1972).

[3] W. Czubatyj and S. J. Hudgens, Invited paper: Thin-film ovonic threshold switch: Its operation and application in modern integrated circuits, Electron. Mater. Lett. **8**, 157 (2012).

[4] T. Prodromakis, C. Toumazou, and L. Chua, Two centuries of memristors, Nat. Mater. **11**, 478 (2012).

[5] B. Chen, F. Cai, J. Zhou, W. Ma, P. Sheridan, and W. D. Lu, in Electron Devices Meeting (IEDM), 2015 IEEE International (IEEE, 2015), pp. 17–15.

[6] Z. Wang, S. Joshi, S. E. Savel'ev, H. Jiang, R. Midya, P. Lin, M. Hu, N. Ge, J. P. Strachan, Z. Li, Q. Wu, M. Barnell, G.-L. Li, H. L. Xin, R. S. Williams, Q. Xia, and J. J. Yang, Memristors with diffusive dynamics as synaptic emulators for neuromorphic computing, Nat. Mater. **16**, 101 (2016).

[7] S. Yu, B. Gao, Z. Fang, H. Yu, J. Kang, and H.-S. P. Wong, Stochastic learning in oxide binary synaptic device for neuromorphic computing, Front. Neurosci. **7**, 186 (2013).

[8] J. del Valle, J. G. Ramírez, M. J. Rozenberg, and I. K. Schuller, Challenges in materials and devices for resistive-switching-based neuromorphic computing, J. Appl. Phys. **124**, 211101 (2018).

[9] A. Sebastian, M. Le Gallo, G. W. Burr, S. Kim, M. BrightSky, and E. Eleftheriou, Tutorial: Brain-inspired computing using phase-change memory devices, J. Appl. Phys. **124**, 111101 (2018).

[10] S. Bagdzevicius, K. Maas, M. Boudard, and M. Burriel, Interface-Type resistive switching in perovskite materials, J. Electroceramics **39**, 157 (2017).

[11] D. Lang and R. Logan, Large-Lattice-Relaxation Model for Persistent Photoconductivity in Compound Semiconductors, Phys. Rev. Lett. **39**, 635 (1977).

[12] J. Z. Li, J. Y. Lin, H. X. Jiang, J. F. Geisz, and S. R. Kurtz, Persistent photoconductivity in $Ga_{1-x}In_xNyAs_{1-y}$, Appl. Phys. Lett. **75**, 1899 (1999).

[13] S. Lany and A. Zunger, Anion vacancies as a source of persistent photoconductivity in II-VI and chalcopyrite semiconductors, Phys. Rev. B **72**, 035215 (2005).

[14] H. Yin, A. Akey, and R. Jaramillo, Large and persistent photoconductivity due to hole-hole correlation in CdS, Phys. Rev. Mater. **2**, 084602 (2018).

[15] Z. Shao, J. Jie, Z. Sun, F. Xia, Y. Wang, X. Zhang, K. Ding, and S.-T. Lee, MoO_3 nanodots decorated CdS nanoribbons for high-performance, homojunction photovoltaic devices on flexible substrates, Nano Lett. **15**, 3590 (2015).

[16] M. Zhang, Z. Shao, T. Jiang, X. Wu, B. Zhang, X. Zhang, F. Xia, and J. Jie, Tuning electrical and Raman scattering properties of cadmium sulfide nanoribbons via surface charge transfer doping, J. Phys. Chem. C **123**, 15794 (2019).

[17] M. Burgelman, P. Nollet, and S. Degrave, Modelling polycrystalline semiconductor solar cells, Thin Solid Films **361–362**, 527 (2000).

[18] See the Supplemental Material at http://link.aps.org/supplemental/10.1103/PhysRevApplied.15.014014 for further results and discussion of device modeling, device testing, and electron microscopy.

[19] J. J. Yang, D. B. Strukov, and D. R. Stewart, Memristive devices for computing, Nat. Nanotechnol. **8**, 13 (2012).

[20] S. Zhang, S. Long, W. Guan, Q. Liu, Q. Wang, and M. Liu, Resistive switching characteristics of MnO_x-based ReRAM, J. Phys. Appl. Phys. **42**, 055112 (2009).

[21] C.-C. Hsu, S.-Y. Wang, Y.-S. Lin, and Y.-T. Chen, Self-Rectifying and interface-controlled resistive switching characteristics of molybdenum oxide, J. Alloys Compd. **779**, 609 (2019).

[22] V. M. Poole, J. Huso, and M. D. McCluskey, The role of hydrogen and oxygen in the persistent photoconductivity of strontium titanate, J. Appl. Phys. **123**, 161545 (2018).

[23] H. Schroeder, V. V. Zhirnov, R. K. Cavin, and R. Waser, Voltage-Time dilemma of pure electronic mechanisms in resistive switching memory cells, J. Appl. Phys. **107**, 054517 (2010).

[24] A. R. Peaker, V. P. Markevich, and J. Coutinho, Tutorial: Junction spectroscopy techniques and deep-level defects in semiconductors, J. Appl. Phys. **123**, 161559 (2018).